machines

MDPI

Article

Multi-Objective Optimization of Structural Parameters of an Ultra-High-Pressure Premixed Abrasive Waterjet Mixing Valve

Huaibei Xie [1,2,3,4,*], Qingliang Zi [1] and Yan Wang [1]

[1] School of Mechatronics Engineering, Anhui University of Science and Technology, Huainan 232001, China
[2] Institute of Intelligent Machines, Hefei Institutes of Physical Science, Chinese Academy of Sciences, Hefei 230031, China
[3] State Key Laboratory of Digital Intelligent Technology for Unmanned Coal Mining, Huainan 232001, China
[4] Anhui Key Laboratory of Mine Intelligent Equipment and Technology, Anhui University of Science and Technology, Huainan 232001, China
* Correspondence: hbxie@aust.edu.cn; Tel.: +86-0554-666-8934

Abstract

The mixing valve is a key component of an ultra-high-pressure premixed abrasive waterjet system, in which the abrasive–water mixing uniformity plays a decisive role in determining the erosion and cutting performance of the jet. The geometric parameters of the mixing chamber inside the valve are therefore critical factors affecting this uniformity. In this study, the liquid–solid two-phase flow within the mixing chamber was numerically investigated using the Eulerian k–ε turbulence model coupled with the Fluent–Rocky DEM approach. Single-factor simulations were first conducted to identify the effective ranges of key structural parameters influencing the mixing performance. Subsequently, a response surface model was established to describe the relationship between the mixing efficiency (ME) and four critical chamber parameters, namely the throat diameter (TD), throat length (TL), abrasive inlet pipe diameter (AD), and the distance between the throat exit and the abrasive inlet pipe center (TE). Based on this model, the optimal structural parameters of the mixing chamber were determined. The results indicate that when TD = 4 mm, TL = 12 mm, AD = 10 mm, and TE = 7 mm, the simulated ME reaches 34.40% $\pm$ 0.49%, which is in close agreement with the predicted value of 34.57%. Experimental validation conducted on a premixed abrasive waterjet test rig shows that the mean absolute relative error between the simulated and measured ME values is 7.54%, which is below the 10% threshold, confirming the reliability and accuracy of the numerical model.

Keywords: ultra-high pressure; mixing chamber; abrasive jet; computational simulation; structural design

Academic Editor: Zhuming Bi

Received: 23 April 2026
Revised: 23 May 2026
Accepted: 25 May 2026
Published: 28 May 2026

Correction Statement: This article has been republished with a minor change. The change does not affect the scientific content of the article and further details are available within the backmatter of the website version of this article.

1. Introduction

Abrasive waterjet (AWJ) technology is a liquid–solid two-phase jet that derives its erosive and cutting capability from the synergistic interaction between high-pressure water and abrasive particles. Due to its excellent cutting performance, broad process adaptability, high cost-effectiveness, and operational safety, AWJ technology has been widely applied in mechanical manufacturing, mining, tunneling, and related industrial fields [1–4]. According to the manner in which water and abrasive are combined, AWJ systems can be classified into premixed and post-mixed types [5]. Compared with post-mixed systems, premixed abrasive waterjets feature a simpler structural configuration, higher kinetic energy transfer efficiency, and lower operating pressure, and have therefore attracted increasing research interest [6]. To further enhance cutting capability and machining efficiency, ultra-high-pressure premixed abrasive waterjet systems have emerged as a major research focus worldwide [7]. However, owing to the technical challenges associated with constructing ultra-high-pressure experimental platforms and the limitations of existing measurement techniques, studies on abrasive–water mixing uniformity and the underlying mixing mechanisms under ultra-high-pressure conditions remain limited, and a systematic theoretical framework has yet to be established.

In ultra-high-pressure premixed abrasive waterjet systems, the mixing valve serves as the core functional component governing overall system performance, and the geometric parameters of the mixing chamber play a decisive role in determining liquid–solid mixing uniformity. The internal flow characteristics within the mixing chamber directly affect abrasive particle acceleration and jet stability, which in turn influence material removal efficiency and machining quality. Consequently, optimizing the mixing chamber geometry and improving liquid–solid mixing uniformity represent effective approaches to addressing the persistent issues of insufficient abrasive kinetic energy and jet instability in ultra-high-pressure premixed abrasive waterjets.

At present, numerous studies have been conducted to investigate the mixing characteristics of abrasive waterjets. Labus reported that the water–abrasive mixing efficiency is strongly dependent on the geometric parameters of the mixing chamber [8]. Based on kinetic energy transfer theory, Hashish systematically analyzed the effects of system pressure as well as mixing chamber length and diameter on abrasive jet mixing efficiency [9]. Momber and Oh et al. developed a mixing efficiency coefficient model, examined the influence of mixing chamber structural parameters on this coefficient, and proposed recommended parameter ranges [10,11]. Zou X. et al. experimentally investigated the effects of abrasive inlet tube and chamber dimensions on abrasive exit velocity and nozzle wear behavior [12]. Nevertheless, experimental approaches alone face inherent limitations in accurately capturing abrasive particle trajectories, energy transfer processes, and turbulent interactions. These limitations constrain in-depth investigation of abrasive waterjet mixing mechanisms. As a result, numerical simulation has become an indispensable tool for studying liquid–solid two-phase flow in abrasive waterjets.

Currently, the primary numerical approaches for modeling liquid–solid two-phase flow include the Euler–Euler and Euler–Lagrange methods. In the Euler–Euler framework, both liquid and solid phases are treated as interpenetrating continua, transforming the two-phase flow problem into one of multiphase mixing and diffusion. Shi et al. applied the Euler–Euler method to simulate dense solid–liquid flow in a centrifugal slurry pump volute and obtained particle concentration distributions indicative of component wear characteristics [13]. Li and Shen investigated gas–solid hydrodynamics in a dual-loop circulating fluidized bed using the Euler–Euler method, with particular emphasis on the influence of drag models [14]. Patro and Dash combined the Euler–Euler method with the kinetic theory of granular flow to develop a model for dilute turbulent gas–solid flow in vertical pipelines, validating the approach through numerical and experimental comparisons [15]. However, this requires substantial computational effort to resolve continuum-scale interphase interactions and is limited in its ability to resolve individual particle trajectories.

In contrast, the Euler–Lagrange approach treats solid particles as a discrete phase. Particle motion is governed by Newton's second law, while the carrier fluid is described by the Navier–Stokes equations. By coupling fluid flow with particle dynamics, this approach enables detailed tracking of individual particle trajectories and their interactions with the flow field. Consequently, the Euler–Lagrange method has been widely employed in studies of gas–solid flows in pneumatic conveying systems, fluidized beds, cyclone separators, as well as liquid–solid two-phase flows in pumps [16]. Zhou et al. used a

CFD–DEM coupling method to numerically investigate flow regime characteristics in vertical pneumatic conveying pipelines [17]. Wei et al. applied CFD–DEM simulations to examine the influence of abrasive volume fraction on the rock-breaking performance of abrasive waterjets [18]. Zhong et al. employed a CFD–DEM approach to analyze the cleaning effectiveness of abrasive waterjets with different nozzle configurations [19].

In parallel with these numerical methodology developments, significant progress has been made in understanding high-pressure water jet dynamics and their implications for jet performance. Yuan et al. studied ice damage characteristics under high-pressure water jet impact and demonstrated that jet impact pressure and energy distribution are highly sensitive to nozzle geometry and standoff conditions, offering insights applicable to the design of mixing chamber geometries [20]. Furthermore, Zhang et al. showed that high-pressure water jet peening can significantly alter the fatigue crack growth behavior of aluminum alloys by modifying surface integrity through controlled jet impact, and revealed the residual stress transformation mechanism under combined ultrasonic peening and waterjet treatment [21,22]. These studies collectively underscore that the uniformity of jet energy distribution—fundamentally governed by abrasive–water mixing quality—is a decisive factor for the effectiveness of high-pressure water jet applications ranging from material removal to surface treatment. In summary, while experimental studies have established qualitative relationships between individual mixing chamber geometric parameters and jet performance, and numerical investigations have demonstrated the advantages of the CFD–DEM approach in capturing particle-level dynamics, a systematic quantitative multi-parameter optimization of mixing chamber geometry under ultra-high-pressure premixed conditions using coupled CFD–DEM and RSM has not been reported. The interactive effects among key geometric parameters—including throat diameter, throat length, abrasive inlet pipe diameter, and throat exit position—on mixing uniformity remain poorly understood, and an experimentally validated optimal design framework is still lacking. Motivated by these gaps, the present study aims to establish a systematic optimization framework for mixing chamber geometry.

Accordingly, in the present study, the Euler–Lagrange approach was employed to numerically investigate the flow field characteristics within the mixing chamber of an ultra-high-pressure premixed abrasive waterjet system. Single-factor simulations were first conducted to determine appropriate parameter ranges, after which the structural parameters of the mixing chamber were optimized using the Response Surface Methodology (RSM). On this basis, the effects of key geometric parameters on abrasive–water mixing uniformity under ultra-high-pressure conditions were systematically analyzed. The results provide theoretical support for elucidating the mixing mechanism of premixed abrasive waterjets and for guiding the structural design of high-performance mixing valves.

2. Materials and Methods

2.1. Geometric Model and Numerical Simulation

2.1.1. Physical Model

As shown in Figure 1, the ultra-high-pressure premixed abrasive waterjet generation system mainly consists of a high-pressure pump, water tank, abrasive tank, and mixing valve. Among these components, the geometric parameters of the mixing chamber within the mixing valve play a decisive role in governing abrasive–water mixing uniformity, which directly determines the erosion and cutting performance of the abrasive jet. To examine the influence of mixing chamber geometry on the liquid–solid mixing process, the physical model illustrated in Figure 2 was developed.

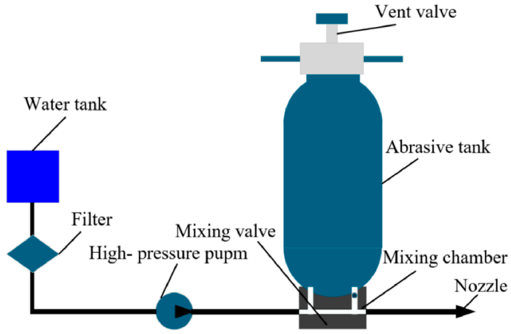

Figure 1. Schematic of the ultra-high-pressure pre-mixed abrasive waterjet generation system.

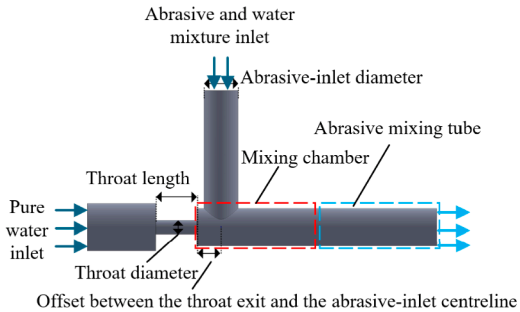

Figure 2. Three-dimensional geometric model of the mixing valve assembly with internal flow passages.

2.1.2. CFD-DEM Coupling Algorithm

In the coupled numerical simulation, the continuous high-pressure water phase is solved using ANSYS Fluent (v 2023 R1), while the abrasive particles (garnet) are tracked using Rocky DEM (v 2023 R1). A two-way coupling strategy is employed to account for momentum exchange between the fluid and particle phases. The overall Fluent–Rocky bidirectional coupling procedure is illustrated in Figure 3.

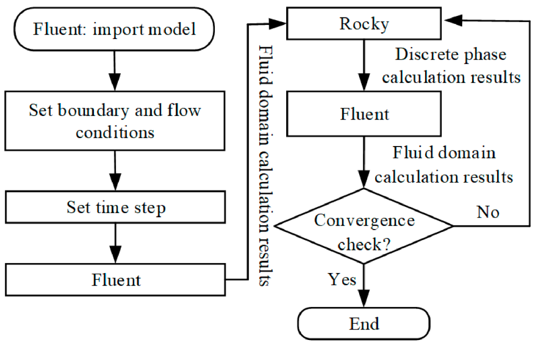

Figure 3. Iterative procedure for the two-way coupled Fluent–Rocky DEM simulation workflow.

2.1.3. Governing Equations

In the early 1970s, Cundall introduced the Discrete Element Method (DEM), which applies Newton's second law to describe particle motion and inter-particle interactions. In this approach, the motion of each individual particle is explicitly tracked, and contact models are used to resolve particle–particle and particle–wall interactions. The macroscopic behavior of the particle assembly is then obtained through the accumulation of microscopic energy and momentum exchange [23]. For the continuous phase, the governing equations consist of the mass continuity equation, the momentum (Navier–Stokes) equations, and the turbulence transport equations based on the k–ε model [24].

Within the DEM framework, each particle undergoes both translational and rotational motion, both of which obey Newton's second law. Particle trajectories and force histories are tracked in a Lagrangian reference frame. The translational motion of a single particle is described by Equation (1) [25].

$$m_p \frac{dv_p}{dt} = m_p g + F_{drag} + F_{loth} + F_P + F_{vm} + F_b + \sum F_c, \tag{1}$$

where F_{drag}, F_{loth}, F_p, F_{vm} and F_b denote the drag force, Saffman lift force, pressure-gradient force, virtual mass force, and buoyancy force acting on the particle, respectively, and F_c represents the contact force arising from particle–particle or particle–wall collisions.

Particle rotation is an essential component of particle dynamics. For relatively large or dense particles with high moments of inertia, rotational effects become particularly significant. Accordingly, the CFD–DEM coupling model accounts for particle rotation induced by tangential contact forces, rolling friction, and hydrodynamic torque. The rotational motion of a single particle is governed by Equation (2).

$$I_P \frac{d\varpi_p}{dt} = \sum T_t + \sum T_r + T_f, \tag{2}$$

where I_p is the particle moment of inertia, ω_p is the angular velocity, and T_c, T_r and T_f denote the torques generated by tangential contact forces, rolling friction, and the surrounding fluid, respectively.

2.1.4. Simulation Setup

The flow field is simulated using ANSYS Fluent, and the computational domain is discretised with unstructured tetrahedral meshes to accurately represent the complex geometry of the mixing chamber. To ensure that the numerical results are not influenced by spatial discretization accuracy, a mesh independence study was carried out. The velocity distribution along a specified line at the outlet of the sand mixing pipe was taken as the evaluation metric; this line extends from point (0.062, 0, 0) to point (0.062, −0.0055, 0). Under fixed boundary conditions and solver settings, four computational meshes with successively increased cell counts were generated. The comparison of the velocity distributions along the specified line for the different meshes is presented in Figure 4. When the mesh was refined from approximately 52,000 cells to 75,000 cells, the velocity distribution showed a noticeable change. However, with further refinement from about 75,000 cells to about 240,000 cells, the velocity distribution remained essentially unchanged, indicating that mesh independence was achieved. Balancing computational efficiency and solution accuracy, the mesh with approximately 75,000 cells was adopted for all subsequent optimization and parametric simulations.

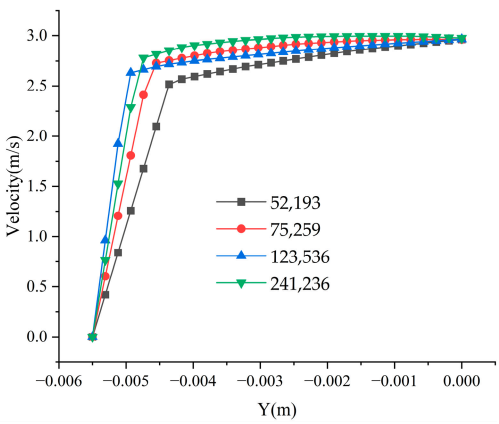

Figure 4. Line graph of velocity variation with mesh count.

Water is defined as the continuous phase, and the Standard k–ε turbulence model is employed to enhance prediction accuracy for strong shear layers and vortical structures. The Standard k–ε model was selected for this study based on its well-established robustness, computational efficiency, and extensive validation for high-Reynolds-number internal flows, which is consistent with the turbulent conditions prevailing in the ultra-high-pressure mixing chamber. While advanced variants such as the RNG k–ε model (which includes an additional term for swirling and rapidly strained flows) and the SST k–ω model (which provides superior near-wall treatment and improved prediction of separated flows) may offer enhanced accuracy for specific flow features, the standard k–ε model is considered adequate for the present objective of evaluating the bulk mixing efficiency, which is governed primarily by global momentum exchange rather than by fine-scale turbulence structures. Both the water inlet and the abrasive–water mixture inlet are specified as velocity inlets, with the inlet velocities determined based on the total volumetric flow rate delivered by the pump system under its rated operating condition, distributed between the two inlets according to their respective cross-sectional areas. This velocity-inlet specification reproduces the mass and momentum flux that corresponds to the experimental operating condition of the ultra-high-pressure system, while the jet outlet is defined as a pressure outlet with standard atmospheric pressure. All solid boundaries are treated as no-slip walls, and the standard wall-function approach is adopted for near-wall turbulence modelling [26].

For the CFD-DEM two-way coupling, the fluid time step was determined to satisfy the Courant–Friedrichs–Lewy condition and the particle relaxation time criterion, while the DEM time step was set as a fraction of the fluid time step to accurately resolve particle–particle and particle–wall collisions. The particle phase is solved using Rocky DEM. Abrasive particles are modelled as spherical garnet grains with a diameter of 0.18 mm, consistent with the abrasives used in the experiments. Table 1 summarizes the density, Poisson's ratio, and Young's modulus of the abrasive particles and wall material used in the DEM contact model. Particle–particle and particle–wall interactions are described using the Hertz–Mindlin nonlinear contact model, which accounts for both normal and tangential contact mechanics. The corresponding contact parameters are listed in Table 2.

Table 1. Physical properties of the garnet abrasive particles and steel wall material adopted in the DEM simulations.

Material	Density ρ/(kg m^{-3})	Poisson's Ratio	Young's Modulus N/m^2
Abrasive	3800	0.25	1×10^8
Wall	7850	0.3	1×10^{11}

Table 2. Hertz–Mindlin contact parameters governing particle–particle and particle–wall interactions.

Interaction	Static Friction Coefficient	Rolling Friction Coefficient	Restitution Coefficient
Abrasive Abrasive	0.3	0.01	0.44
Abrasive Wall	0.5	0.01	0.50

It should be noted that abrasive particles are treated as non-breakable spheres in the present simulations. This simplification is justified on the following grounds. First, garnet abrasive (Mohs hardness 7.5–8.0) possesses high fracture toughness, and despite the ultra-high pressures, fragmentation is unlikely due to short residence time. Second, the primary objective of this study is to evaluate abrasive–water mixing uniformity, which is governed predominantly by momentum exchange and turbulent dispersion rather than by particle breakage. Moreover, Li et al. demonstrated the effects of the Tavares breakage model, which has been successfully implemented in Rocky DEM to capture body breakage of brittle materials, on grinding kinetics and fragment distribution in DEM simulations [27]. While incorporating such a breakage model could provide additional insights into abrasive degradation phenomena, it would substantially increase model complexity and computational cost. Therefore, the non-breakable particle assumption is considered reasonable for the present scope, and the potential influence of particle breakage is recommended for investigation in future studies employing the Tavares breakage model.

2.2. Single-Factor Experiment

2.2.1. Single-Factor Simulation Experiment

Based on previous studies and preliminary investigations conducted by the research group, it was determined that the mass ratio (MR), throat diameter (TD), throat length (TL), abrasive inlet pipe diameter (AD), and throat exit-to-abrasive inlet pipe center distance (TE) are the key factors affecting abrasive–water mixing uniformity within the mixing chamber [28–30]. Accordingly, these five parameters were selected as the critical structural variables for the single-factor numerical simulations, with the objective of systematically evaluating their influence on abrasive distribution uniformity. To quantitatively characterize the mixing uniformity between abrasive particles and water, the mixing efficiency (ME) was adopted as the evaluation index, following the mixing quality quantification approaches employed in prior abrasive waterjet studies. The ME, defined by Equations (3)–(5) as the percentage ratio of the total cross-sectional area occupied by abrasive particles to the total area of the mixing chamber outlet, expressed as a percentage. The outlet section corresponds to the region where the abrasive–water mixture has fully developed into a turbulent flow.

$$A_1 = \frac{\pi d_0^2}{4}, \tag{3}$$

$$A_2 = \frac{\pi d^2}{4}, \tag{4}$$

$$\psi = \frac{NA_1}{A_2} \times 100\%, \tag{5}$$

where d_0 is the abrasive particle diameter (mm), d is the diameter of the outlet cross-section (mm), A_1 is the cross-sectional area of a single abrasive particle (mm^2), A_2 is the cross-sectional area of the mixing chamber outlet (mm^2), N is the number of particles passing through the outlet cross-section, and ψ represents the mixing efficiency (%).

Considering both the results of preliminary investigations and the constraints of the available experimental equipment, the parameter ranges for the single-factor numerical simulations were defined as follows: mass ratio (MR) of 15–30%, throat diameter (TD) of 3.5–5 mm, throat length (TL) of 12–18 mm, abrasive inlet pipe diameter (AD) of 8–11 mm, and throat exit-to-abrasive inlet pipe center distance (TE) of 6–9 mm. Based on these ranges, a single-factor simulation scheme was adopted, and the detailed parameter levels are listed in Table 3.

Table 3. Factor-level layout for the single-factor numerical simulation scheme.

Factor	Parameter			
MR (%)	15	20	25	30
TD (mm)	3.5	4	4.5	5
TL (mm)	12	14	16	18
AD (mm)	8	9	10	11
TE (mm)	6	7	8	9

2.2.2. Single-Factor Experimental Results

Based on the numerical simulation results, the temporal evolution of the number of abrasive particles passing through the outlet cross-section of the mixing chamber was obtained, as shown in Figure 5. Specifically, Figure 5a–e illustrate the effects of MR, TD, TL, AD, and TE on the particle number at the outlet, respectively.

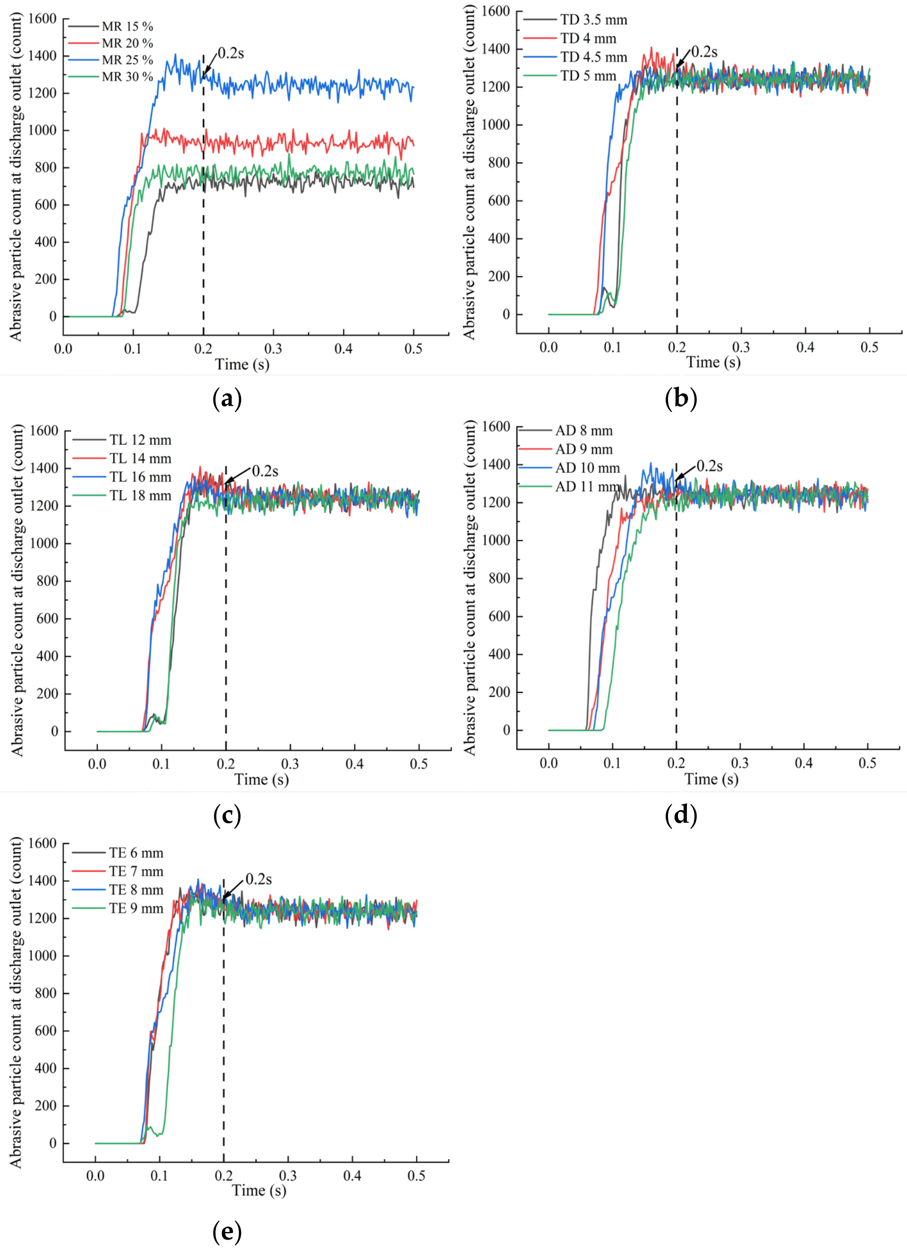

Figure 5. Time-series profiles of the cumulative number of abrasive particles exiting the mixing chamber as functions of: (**a**) mass ratio (MR), (**b**) throat diameter (TD), (**c**) throat length (TL), (**d**) abrasive inlet pipe diameter (AD), and (**e**) throat exit distance (TE).

To further analyze the motion behavior of abrasive particles, a representative operating condition (MR = 25%, TD = 4.5 mm, TL = 14 mm, AD = 10 mm, TE = 8 mm) was selected from Figure 5. The corresponding particle motion states at different time instants are shown in Figure 6.

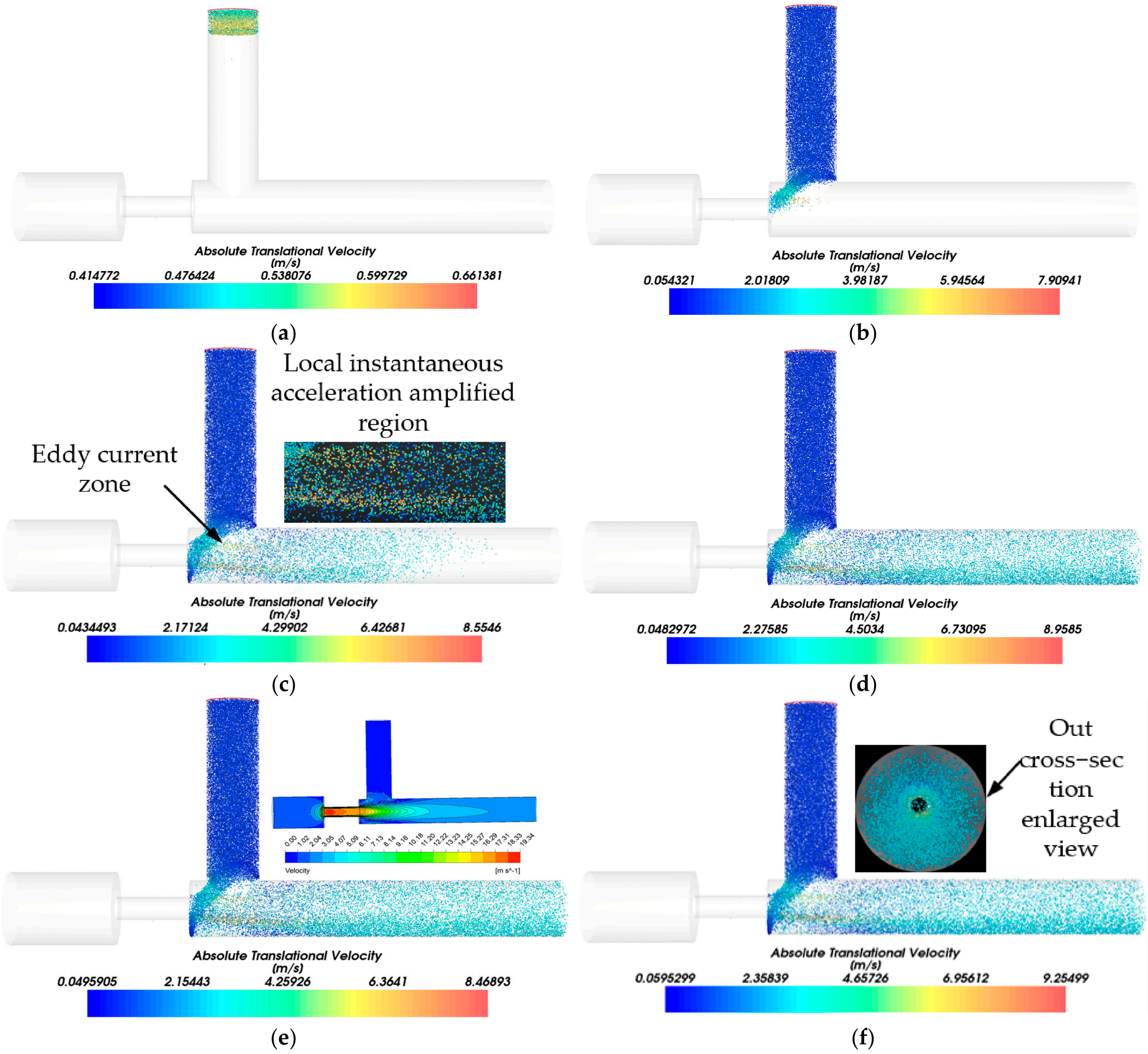

Figure 6. Snapshots of the abrasive particle spatial distribution superimposed with velocity magnitude contours at six characteristic instants during the mixing process. (**a**) T = 0.01 s. (**b**) T = 0.062 s. (**c**) T = 0.074 s. (**d**) T = 0.12 s. (**e**) T = 0.15 s. (**f**) T = 0.2 s.

As shown in Figure 6, at T = 0.01 s, the abrasive–water mixture enters the mixing chamber. At T = 0.062 s, a negative-pressure region forms in the upper-left region of the chamber. This is caused by the interaction between the high-pressure water jet at the throat exit and the mixture entering from the abrasive inlet pipe. Under the combined effects of negative pressure and gravity, the mixture is transported toward the throat exit. At T = 0.074 s, a vortex structure develops around the high-pressure water jet. Part of the abrasive is entrained into the core of the jet and undergoes rapid acceleration, while the remaining abrasive is dispersed and mixed with the water under vortex-induced turbulent motion, significantly enhancing particle dispersion. As time progresses to T = 0.12 s, the jet velocity in the core region decreases, and the vortex region further expands, leading to improved abrasive dispersion within the chamber. After T = 0.15 s, the abrasive–water mixing process gradually reaches a statistically stable state. To further clarify the jet–particle interaction, velocity magnitude contours at the corresponding time instants were added to Figure 6 alongside the particle cloud diagrams. The contours reveal a high-velocity central jet core that rapidly entrains the surrounding abrasive particles and accelerates them along the axial direction. In contrast, the low-velocity regions near the chamber walls are associated with recirculation zones, where particles are captured by vortices and undergo turbulent dispersion before being drawn back into the jet core. This visual evidence confirms that the momentum transfer from the high-speed water jet to the abrasive particles is the primary mechanism governing mixing uniformity. The schematic distribution of abrasive particles at the outlet cross-section is shown in Figure 6f.

To evaluate the ME under stable mixing conditions, three time intervals of equal duration—0.25–0.35 s, 0.30–0.40 s, and 0.35–0.45 s—were selected after the flow reached a turbulent steady state. The average particle number within these intervals was calculated, and the corresponding ME values were used to generate the parameter influence curves shown in Figure 7.

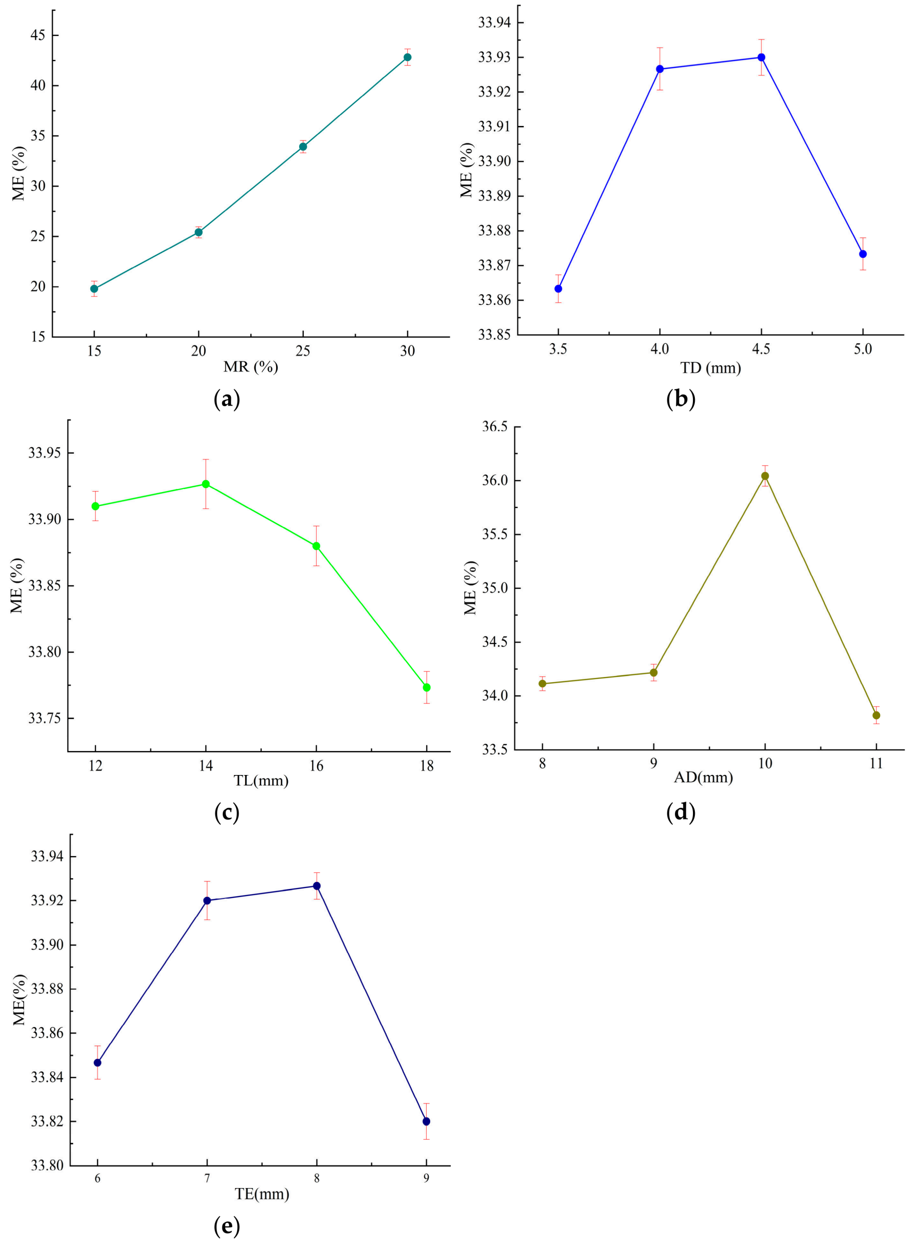

Figure 7. Influence of the five key parameters on the mixing efficiency: (**a**) mass ratio, (**b**) throat diameter, (**c**) throat length, (**d**) abrasive inlet pipe diameter, and (**e**) throat exit-to-abrasive inlet pipe center distance.

In ultra-high-pressure waterjet systems, the impact behavior of the high-speed jet is known to be highly sensitive to nozzle geometry and standoff conditions, as recently demonstrated by Yuan et al. in a study on ice damage characteristics [20]. Their work reveals that variations in geometric parameters significantly alter the jet impact pressure and energy distribution, which in turn governs the material removal and fragmentation processes. These insights are transferable to the present mixing chamber, where the high-pressure water jet entrains and accelerates abrasive particles: the momentum exchange efficiency between the jet and the particles is strongly influenced by throat dimensions and the relative position of the abrasive inlet, analogous to the geometry-dependent jet impact dynamics reported by Yuan et al.

As shown in Figure 7a, the ME increases monotonically with increasing MR. At low MR values, the impact force of the abrasive jet is insufficient, reducing erosion and cutting efficiency. Although higher MR values enhance jet impact capacity, excessively large MR values are constrained by abrasive tank capacity and operational duration. Therefore, an MR of 25% is considered optimal.

As shown in Figure 7b, when TD increases from 3.5 mm to 4.5 mm, the ME increases and reaches a maximum at TD = 4.5 mm. Further increasing TD leads to a decline in ME. For small TD values, the excessive jet velocity causes premature abrasive acceleration and insufficient residence time for mixing. In contrast, overly large TD values reduce jet velocity, causing abrasive particles to settle under gravity and deteriorating mixing quality. Accordingly, TD values in the range of 4–5 mm are recommended.

As shown in Figure 7c, the ME initially increases with increasing TL, reaches a maximum at TL = 14 mm, and then gradually decreases as TL increases further. When the throat length is short, the residence time of abrasive particles is insufficient for the high-speed water jet to fully accelerate them to a velocity close to that of the water phase; the particle velocity distribution remains broad, leading to non-uniform particle dispersion across the outlet cross-section and a low ME. As TL increases, the acceleration path is extended, allowing more particles to approach the water velocity under the continuous drag of the jet, while the developing turbulent structures in the mixing chamber promote particle dispersion, both of which improve ME. However, beyond the optimum TL, the wall friction along the elongated throat causes a noticeable total-pressure loss and a decay in the water-jet velocity, weakening the drag force on the particles. The longer flow path also increases the probability of particle–particle and particle–wall collisions, resulting in additional dissipation of particle kinetic energy, and may even induce local particle settling due to gravity. These combined effects lead to a decline in ME. Therefore, a TL range of 12–16 mm is considered appropriate.

As shown in Figure 7d, the ME increases with AD from 8 mm to 10 mm, reaching a peak at AD = 10 mm, and then decreases when AD is further increased. A small AD restricts abrasive supply and may cause a starved-feeding condition, whereas an excessively large AD intensifies pressure fluctuations and leads to non-uniform abrasive intake. Consequently, AD values between 9 mm and 11 mm are recommended.

As shown in Figure 7e, the ME increases as TE increases from 6 mm to 8 mm and reaches a maximum at TE = 8 mm. Further increases in TE result in a pronounced decrease in ME. When TE is too small, abrasive particles are directly impacted by the high-pressure jet shortly after entering the chamber, leading to localized accumulation. Conversely, excessively large TE values promote particle settling and insufficient dispersion, resulting in non-uniform mixing. Therefore, TE values in the range of 7–9 mm are considered optimal.

2.3. Response Surface Analysis and Optimization

2.3.1. Box Behnken Experimental Design

Response Surface Methodology (RSM), which is widely used to establish quantitative relationships between response variables and control factors, has been extensively applied in structural optimization studies [31]. Based on the results of the single-factor numerical simulations, four key parameters—throat diameter (TD, A), throat length (TL, B), abrasive inlet pipe diameter (AD, C), and throat exit-to-abrasive inlet pipe center distance (TE, D)—were selected as independent variables. The mixing efficiency (ME, Y) was adopted as the response variable to characterize abrasive–water mixing uniformity within the mixing chamber.

With the objective of maximizing ME, a four-factor, three-level Box–Behnken Design (BBD) was employed, as summarized in Table 4. It should be noted that the mass ratio (MR) was not included as an independent variable in the RSM optimization. MR is an operational parameter rather than a geometric design parameter of the mixing chamber. The single-factor analysis indicated that ME increases monotonically with MR within the tested range, and a value of 25% was selected as optimal based on practical constraints related to abrasive tank capacity and operation duration. Consequently, MR was fixed at 25% for all subsequent structural optimization simulations, allowing the RSM analysis to focus exclusively on the four key geometric parameters (TD, TL, AD, and TE) that directly govern the mixing chamber design. The response surface model relating the key structural parameters of the mixing chamber to ME was established using Design-Expert 13.0 software. Numerical simulations were subsequently performed for each design point to obtain the corresponding ME values. The complete BBD matrix and simulation results are presented in Table 5. The statistical significance and adequacy of the regression model were evaluated through analysis of variance (ANOVA), and a second-order polynomial regression equation describing the relationship between the structural parameters and ME was obtained.

Table 4. Coded and actual levels of the independent variables in the four-factor Box–Behnken design.

Symbols	Input Variables	Units	Levels		
			Low (−1)	Medium (0)	High (+1)
A	TD	mm	4	4.5	5
B	TL	mm	12	14	16
C	AD	mm	9	10	11
D	TE	mm	7	8	9

Table 5. Box–Behnken design matrix with the CFD–DEM simulated mixing efficiency (ME) as the response variable.

No.	Input Parameters				Output Response
	A	B	C	D	ME (Y)
1	−1	−1	0	0	34.41
2	1	−1	0	0	34.10
3	−1	1	0	0	34.14
4	1	1	0	0	33.79
5	0	0	−1	−1	34.26
6	0	0	1	−1	33.23
7	0	0	−1	1	34.09
8	0	0	1	1	33.80
9	−1	0	0	−1	34.40
10	1	0	0	−1	34.33
11	−1	0	0	1	34.18
12	1	0	0	1	33.86
13	0	−1	−1	0	34.19
14	0	1	−1	0	34.18

Table 5. *Cont.*

No.	Input Parameters				Output Response
	A	B	C	D	ME (Y)
15	0	−1	1	0	33.82
16	0	1	1	0	33.54
17	−1	0	−1	0	34.33
18	1	0	−1	0	34.15
19	−1	0	1	0	34.10
20	1	0	1	0	33.33
21	0	−1	0	−1	34.55
22	0	1	0	−1	34.28
23	0	−1	0	1	34.18
24	0	1	0	1	33.87
25	0	0	0	0	34.02
26	0	0	0	0	34.00
27	0	0	0	0	33.95
28	0	0	0	0	34.08
29	0	0	0	0	33.87

2.3.2. Box Behnken Experimental Results

Using TD (A), TL (B), AD (C), and TE (D) as independent variables and ME (Y) as the response, a quadratic regression model was fitted to the data in Table 5 using Design-Expert software. The resulting regression equation is expressed as Equation (6).

$$\begin{aligned} Y = &+0.407A^2 + 0.02325B^2 - 0.16075C^2 + 0.0905D^2 \\ &-0.01AB - 0.285AC - 0.125AD - 0.03375BC - 0.005BD + 0.185CD \\ &+0.093667A - 0.288917B + 3.25333C - 2.75467D + 33.48558 \end{aligned} \quad (6)$$

The ANOVA results, listed in Table 6, show that the model F-value is 6.01 with a corresponding p-value of 0.0009, indicating that the regression model is statistically significant. The coefficient of determination (R^2 = 0.8573) demonstrates a reasonable between the predicted and simulated ME values, explaining approximately 85.73% of the response variability. In the context of CFD-DEM coupled simulations for solid–liquid two-phase flow, where inherent numerical fluctuations arise from complex momentum exchange, turbulence, and particle–particle collisions, a moderate R^2 value is considered acceptable and indicates reasonable predictive capability. The adjusted coefficient of determination (R^2 Adj = 0.7147) is reasonably close to R^2, and the lack-of-fit is not significant (p = 0.0567 > 0.05), which confirms the model's adequacy and robustness within the investigated parameter space. Among the linear terms, A (TD) and C (AD) exhibit highly significant effects on ME (p < 0.01), whereas B (TL), the quadratic term C^2, and the interaction term CD are statistically significant at the p < 0.05 level. Based on the F-values and p-values, the relative influence of the four parameters on ME can be ranked as: C > A > B > D. The normal probability plot of the residuals, shown in Figure 8a, indicates that the residuals follow an approximately normal distribution, confirming the validity of the regression assumptions. In addition, the strong linear correlation between predicted and simulated ME values in Figure 8b demonstrates the high predictive accuracy of the developed response surface model.

To visualize the interactive effects of TD (A), TL (B), AD (C), and TE (D) on ME, three-dimensional response surface plots and corresponding contour maps were generated, as shown in Figure 8. According to the ANOVA results in Table 6, parameters A, B, and C, as well as the interaction term CD, exert significant influences on ME. Among them, AD (C) exhibits the strongest effect, consistent with its highest F-value.

Table 6. Analysis of variance (ANOVA) for the quadratic regression model of mixing efficiency.

Items	Sum of Squares	DOF	Mean Square	F-Value	*p*-Value
Model	2.22	14	0.1588	6.01	0.0009
A	0.3333	1	0.3333	12.61	0.0032
B	0.1752	1	0.1752	6.63	0.0220
C	0.9520	1	0.9520	36.02	<0.0001
D	0.0954	1	0.0954	3.61	0.0782
AB	0.0004	1	0.0004	0.0151	0.9038
AC	0.0870	1	0.0870	3.29	0.0911
AD	0.0156	1	0.0156	0.5911	0.4558
BC	0.0182	1	0.0182	0.6895	0.4203
BD	0.0004	1	0.0004	0.0151	0.9038
CD	0.1369	1	0.1369	5.18	0.0391
A^2	0.0672	1	0.0672	2.54	0.1333
B^2	0.0561	1	0.0561	2.12	0.1672
C^2	0.1676	1	0.1676	6.34	0.0246
D^2	0.0531	1	0.0531	2.01	0.1782
Residual	0.3701	14	0.0264		
Lack of Fit	0.3451	10	0.0345	5.54	0.0567
Pure Error	0.0249	4	0.0062		
Cor Total	2.59	28			
	$R^2 = 0.8573$ $R^2_{Adj} = 0.7147$				

Note: R^2 = 0.8573, Adj. R^2 = 0.7147.

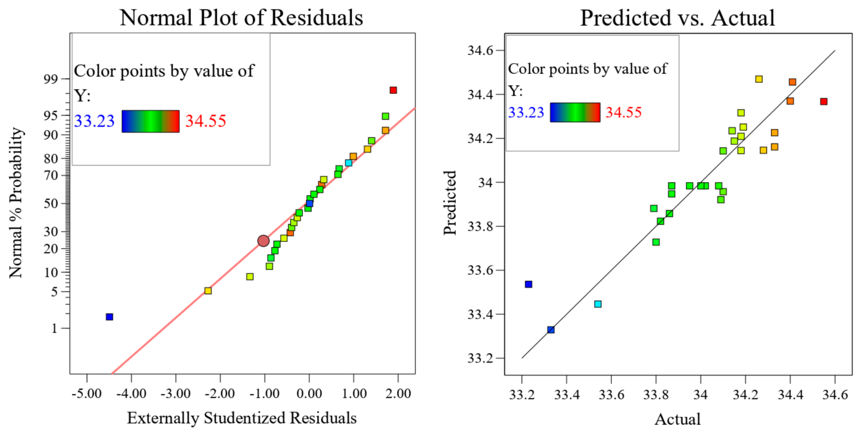

(**a**) (**b**)

Figure 8. Model adequacy diagnostics: (**a**) normal probability plot of the studentized residuals; (**b**) parity plot of the predicted versus CFD–DEM simulated mixing efficiency values.

As shown in Figure 9a–c, when A is small, the velocity of the high-pressure water jet increases markedly. This leads to more frequent and intense collisions between abrasive particles and the inner wall of the mixing chamber. This enhanced collision activity leads to substantial energy dissipation of the abrasive particles, thereby reducing the uniformity of the abrasive–water mixture and decreasing the mixing efficiency (ME). In contrast, when A is large, the kinetic energy of the water jet becomes overly dispersed, and variations in C no longer contribute significantly to improving the mixing uniformity.

As illustrated in Figure 9a,d,e, the ME first decreases and then increases with increasing B. At small values of B, the residence time of abrasive particles within the mixing chamber is insufficient to allow thorough mixing with water, resulting in a low ME. As B increases, mixing improves; however, excessively large B values increase flow resistance, reduce jet velocity, and promote secondary collisions among abrasive particles. These effects enhance internal energy dissipation within the abrasive phase and ultimately lead to a decline in ME.

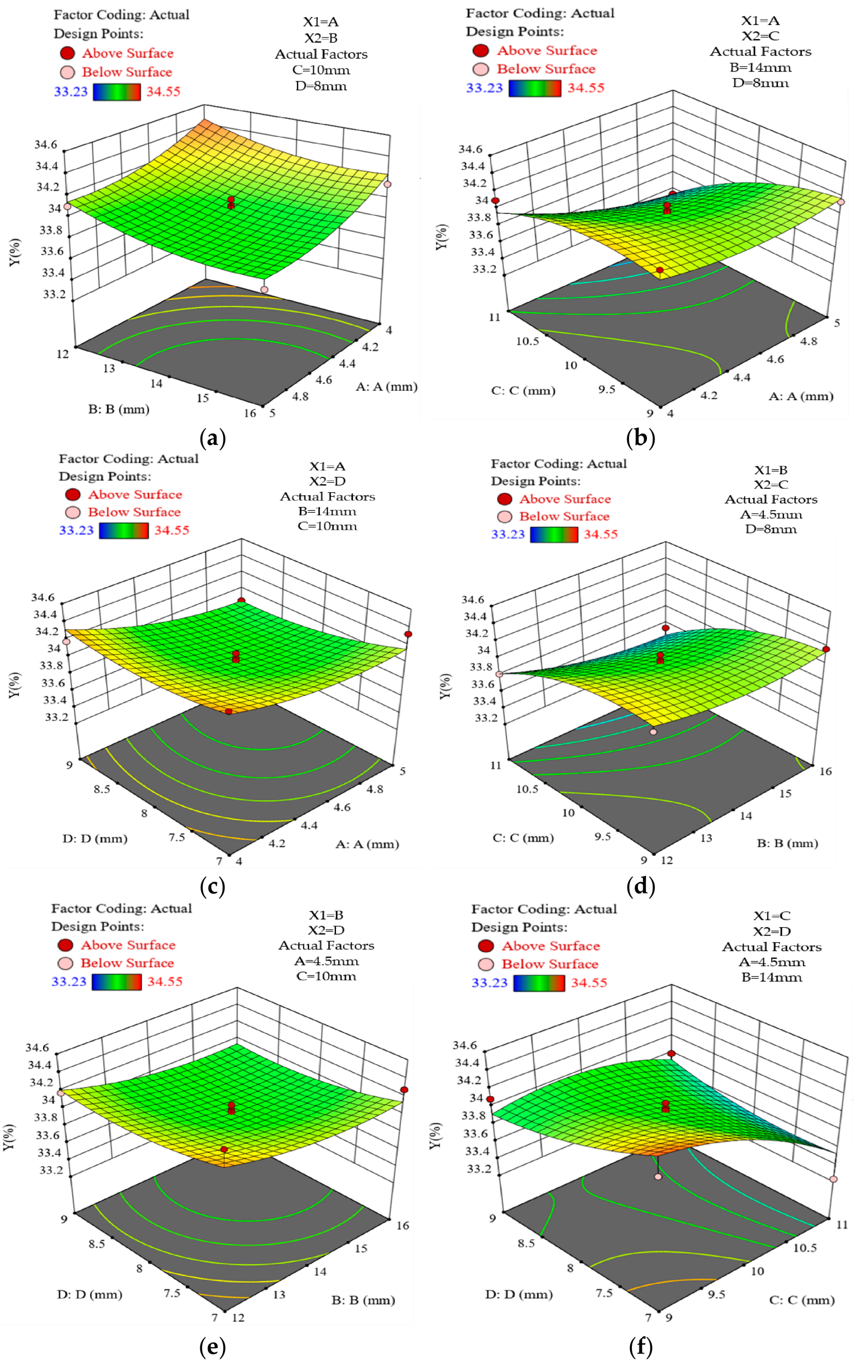

Figure 9. Three-dimensional response surface plots and corresponding contour maps illustrating the pairwise interactive effects on mixing efficiency: (**a**) TD and TL; (**b**) TD and AD; (**c**) TD and TE; (**d**) TL and AD; (**e**) TL and TE; (**f**) AD and TE.

As shown in Figure 9b,d,f, the ME initially increases and then decreases with increasing C. When C is small, the abrasive mass flow rate entering the mixing chamber through the inlet pipe is limited, leading to insufficient abrasive participation in the mixing process and a reduced ME. Conversely, excessively large C values result in an overconcentration of abrasive particles, causing local particle settling within the mixing chamber and deteriorating mixing uniformity.

As shown in Figure 9c,e,f, the ME exhibits a slight decrease followed by an increase as D increases. When D is small, abrasive particles are rapidly entrained by the high-pressure water jet and exit the mixing chamber shortly after entering, leaving insufficient time for effective mixing. With increasing D, the residence time of abrasive particles increases, improving mixing uniformity. However, excessively large D values promote particle settling due to gravity, which hinders effective mixing and leads to a reduction in ME.

Figure 9 further indicates that the relative influence of the four parameters on the ME follows the order C > A > B > D. Although C has the most significant effect and D the least, the interaction between C and D remains statistically significant. These observations are consistent with the ANOVA results presented in Table 6.

Based on the parameter ranges of throat diameter (TD), throat length (TL), abrasive inlet pipe diameter (AD), and throat exit–to–abrasive inlet pipe center distance (TE), together with the target ME specified in Table 7, the RSM–BBD model was employed to determine optimal parameter combinations. A total of 25 candidate optimal structural parameter sets were obtained, as listed in Table 8. To validate the predictive capability of the response surface model, five parameter sets were randomly selected for numerical simulation, and the corresponding ME values were calculated. It should be noted that all 25 candidate combinations listed in Table 8 are located within a narrow high-desirability region of the parameter space, and their predicted ME values are therefore very close to one another. The five validation cases were selected to represent different parts of this near-optimal region and to test whether the response surface model remained accurate after numerical re-simulation, rather than to identify a single best combination. The final rounded design was chosen by considering multiple factors, including the RSM-predicted ME, the validation simulation error, manufacturability, and parametric robustness, rather than by desirability alone. A comparison between the predicted and simulated results is presented in Table 9, showing that the relative errors are all below 5%, thereby confirming the reliability and accuracy of the developed model.

Table 7. Optimization constraints and target criterion specified for the desirability function.

Parameters	Confidence Lower Limit	Confidence Upper Limit	Importance
TD (mm)	4	5	3
TL (mm)	12	16	3
AD (mm)	9	11	3
TE (mm)	7	9	3
ME (%)	33.23	34.55	3

According to the regression model and the validation results in Table 9, the parameter combination yielding the smallest relative error was selected as the optimal configuration: TD = 4.012 mm, TL = 12.171 mm, AD = 9.744 mm, and TE = 7.067 mm, with a predicted ME of 34.57%. Considering manufacturing feasibility, these parameters were rounded to TD = 4 mm, TL = 12 mm, AD = 10 mm, and TE = 7 mm. A numerical simulation was subsequently conducted using the rounded parameters. The temporal variation in outlet mass flow is shown in Figure 10, from which the simulated ME was calculated as 34.40% $\pm$ 0.49%. The relative error between the simulated and predicted values is less than 1%. To assess the robustness of the rounded optimal parameters against manufacturing tolerances, the sensitivity of ME to small perturbations around the optimum was examined. As shown in the single-factor curves, the ME remains relatively flat within the recommended ranges. This insensitivity confirms that the rounded optimum resides in a robust region of the parameter space where small manufacturing-induced deviations will not significantly compromise the mixing efficiency, further validating the effectiveness of the proposed optimization model.

Table 8. Candidate optimal parameter sets sorted by the RSM desirability function.

No	TD	TL	AD	TE	ME	Desirability
1	4.476	12.240	9.104	7.005	34.556	1
2	4.047	12.098	9.374	7.170	34.550	1
3	4.010	12.296	9.060	7.188	34.557	1
4	4.901	12.113	9.040	7.009	34.688	1
5	5.000	12.031	9.096	7.086	34.604	1
6	4.043	12.486	9.075	7.051	34.577	1
7	4.931	14.926	9.047	7.018	34.554	1
8	4.008	12.016	9.559	7.318	34.558	1
9	4.970	14.344	9.056	7.023	34.565	1
10	4.759	12.715	9.030	7.008	34.580	1
11	4.574	12.399	9.098	7.014	34.555	1
12	4.000	12.001	10.308	8.997	34.550	1
13	4.147	12.167	9.250	7.040	34.582	1
14	4.981	13.069	9.183	7.027	34.585	1
15	4.015	12.998	9.048	7.026	34.555	1
16	4.012	12.171	9.744	7.067	34.573	1
17	4.000	12.000	10.199	8.998	34.547	0.998
18	4.000	12.000	10.541	8.967	34.538	0.991
19	4.000	12.096	10.345	9.000	34.536	0.990
20	4.000	12.000	10.000	9.000	34.530	0.985
21	4.000	14.246	9.000	7.000	34.525	0.981
22	4.000	12.020	10.164	8.884	34.523	0.979
23	4.004	12.000	10.160	7.000	34.517	0.975
24	4.131	14.740	9.000	7.000	34.493	0.956
25	4.001	12.000	9.927	8.546	34.470	0.939

Table 9. Comparison between the RSM-predicted and the CFD–DEM simulated mixing efficiency for the five validation cases.

No.	TD	TL	AD	TE	RMS Predicted Value (%)	Simulated Value (%)	Relative Error (%)
1	4.476	12.240	9.104	7.005	34.56	34.13	1.26
2	4.043	12.486	9.075	7.051	34.58	33.99	1.74
3	4.574	12.399	9.098	7.014	34.56	34.14	1.23
4	4.012	12.171	9.744	7.067	34.57	34.40	0.49
5	4.000	14.246	9.000	7.000	34.53	34.04	1.44

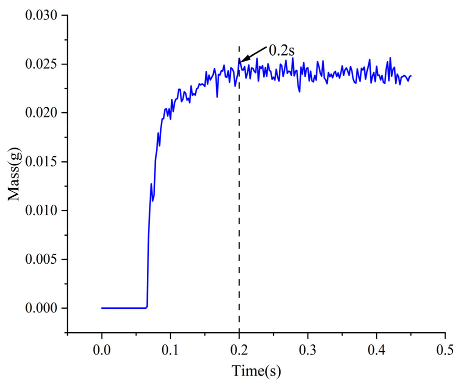

Figure 10. Transient evolution of the abrasive mass flow rate at the mixing chamber outlet under the optimal parameter configuration.

3. Results

3.1. Verification Testing

3.1.1. Experimental Equipment

To validate the accuracy of the numerical simulation results, an experimental platform for measuring the mixing efficiency was established. The platform mainly consists of a computer numerical control (CNC) system, a cutting platform, a pre-mixed abrasive waterjet (AWJ) generation device, a pump station system, a weight measurement unit, and a laptop computer. The pre-mixed AWJ generation device includes an abrasive tank and a mixing valve, whereas the pump station system is composed of a water tank, a high-pressure pump, a pressure-regulating valve, and a power control unit. A schematic diagram of the experimental setup is shown in Figure 11.

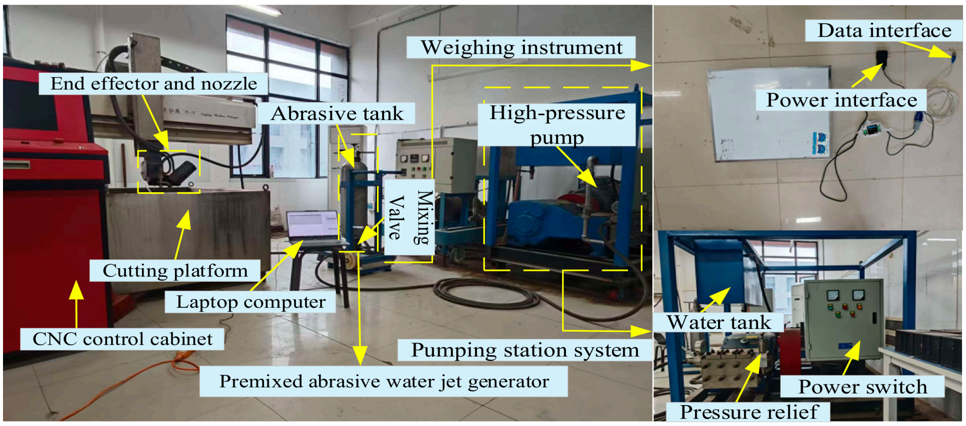

Figure 11. Schematic configuration of the experimental test rig designed for mixing efficiency measurement and validation.

3.1.2. Mixing Efficiency Measurement

During the experiment, the abrasive tank was filled with garnet abrasive, and the weight measurement unit was positioned beneath the pre-mixed abrasive waterjet generation system. After the system was powered on and the data acquisition interface was connected to the computer, the pump station was activated. Once the system reached a stable operating state, the abrasive valve was opened.

The weight measurement unit continuously recorded the variation in abrasive mass in real time and transmitted the data to the computer. Based on the measured data, three time-dependent curves of abrasive mass under different operating conditions were obtained, as shown in Figure 12. The average abrasive mass variations within a 1 s interval were 13.5 g, 12.5 g, and 11 g, respectively.

3.1.3. Comparison Between Simulation and Experiment

According to the time-dependent outlet mass curve obtained from the numerical simulation under the optimal structural parameters (Figure 10), the outlet mass stabilized after approximately 0.2 s. Using a sampling interval of 0.002 s, the average outlet abrasive mass was calculated as 0.0245 g, corresponding to an abrasive mass of 12.25 g within 1 s. The resulting simulated mixing efficiency was 34.40%.

The experimental mixing efficiency values were derived from the measured abrasive mass data through a proportional scaling procedure, as expressed in Equation (7). Since the mixing efficiency is directly proportional to the abrasive mass flow rate under fixed operating conditions, the simulated relationship between the average outlet abrasive mass (12.25 g within 1 s) and the corresponding ME (34.40%) was used as the calibration reference. For each experimental run, the ME was therefore calculated as the product of the measured-to-simulated mass ratio and the simulated ME. Applying this procedure to the three experimentally measured abrasive masses (13.5 g, 12.5 g, and 11 g) yields the corresponding ME values of 37.91%, 35.10%, and 30.89%, respectively, as reported in Table 10.

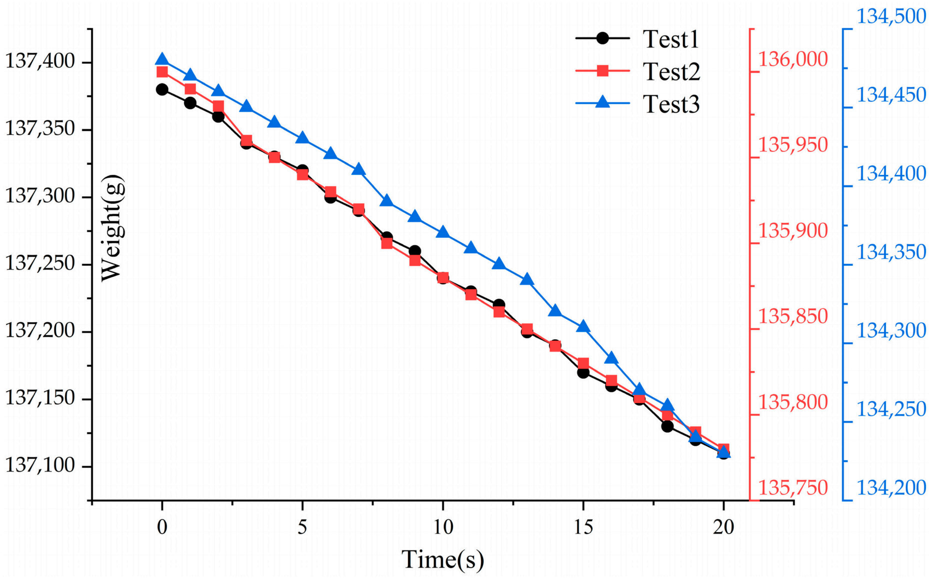

Figure 12. Experimentally acquired temporal profiles of accumulated abrasive mass for three independent measurement runs.

Table 10. Experimentally measured abrasive mass and the corresponding mixing efficiency values with relative error analysis.

Run	Test1	Test2	Test3
Abrasive weight (g)	13.5	12.5	11
Y_{test} (%)	37.91	35.10	30.89
Error (%)	9.26	1.99	11.36
Mean Absolute Error (%)		7.54	

The average absolute relative error between the simulated and experimental mixing efficiency values was 7.54%, which is within the acceptable error range for experimental validation. The individual errors for the three test runs ranged from 1.99% to 11.36%. This variation reflects the inherent fluctuations in abrasive feeding and flow conditions during independent experimental runs of the ultra-high-pressure system. The 7.54% average absolute error is therefore interpreted as a summary indicator of the overall model accuracy, rather than the sole measure of validation performance. Despite the spread, the mean error remains below the 10% threshold, confirming the general reliability of the numerical model.

$$\frac{m_{Test}}{m_{\text{Fluid}}} = \frac{\varphi_{\text{Fluid}}}{\varphi_{Test}}, \quad (7)$$

4. Discussion

4.1. Comparison with Previous AWJ Mixing Studies

The optimal mixing chamber configuration identified in the present study (TD = 4 mm, TL = 12 mm, AD = 10 mm, TE = 7 mm) is consistent in trend with the design recommendations reported in previous abrasive-waterjet studies, although it differs quantitatively due to the ultra-high-pressure premixed configuration adopted here. Hashish and Momber & Kovacevic established, on the basis of kinetic-energy transfer theory, that the throat diameter and throat length jointly govern the momentum exchange between the high-pressure water jet and the abrasive particles, and that a non-monotonic relationship between throat geometry and jet performance exists—an observation directly reproduced by our single-factor curves in Figure 7 [9,10]. Oh and Cho similarly identified an optimum mixing-tube diameter for rock-cutting AWJ, beyond which the kinetic-energy transfer efficiency rapidly deteriorates, in agreement with the ME decline we observed for TD > 4.5 mm [11]. In post-mixed AWJ systems, Zou et al. reported that an excessively large abrasive inlet pipe diameter intensifies pressure fluctuations and reduces particle exit velocity; the present results confirm that the same physical mechanism operates in premixed ultra-high-pressure configurations, with an optimal AD value near 10 mm [12]. Quantitative differences—for example, our shorter optimal TL (12 mm) compared with the 50–100 mm focusing tubes typical of injection-type AWJ studies [11,12]—are attributable to the fundamentally different mixing mode: in premixed AWJ the abrasive and water are already partially mixed upstream, so wall-friction-induced momentum loss becomes the dominant penalty once the throat is sufficiently long, rather than the abrasive-acceleration deficit that governs injection-type designs.

4.2. Novel Contribution: AD–TE Interaction

A statistically significant interaction between AD and TE (CD term, F = 5.18, $p = 0.0391$) was identified in the present RSM analysis, indicating that the influence of the abrasive inlet pipe diameter on ME is contingent upon the throat exit-to-inlet distance. To the best of our knowledge, this coupled effect has not been systematically reported in previous studies on AWJ mixing chamber design. Single-factor investigations addressed each geometric parameter in isolation; RSM optimisations of AWJ machining parameters (e.g., traverse speed, pressure, abrasive flow rate) by Liu and Fuse et al. focused on operational rather than geometric variables [32,33]. The CFD–DEM study of Zou et al. [12] varied AD and chamber length independently without analysing their interaction. The physical origin of the AD–TE coupling identified in the present work can be interpreted as follows: AD governs the abrasive mass flow rate entering the chamber, while TE governs the time available for the incoming abrasive to disperse before being entrained by the high-pressure jet. When AD is large (high abrasive feed rate) and TE is simultaneously large (long pre-entrainment distance), gravitational settling becomes dominant before the jet captures the particles—producing the steep ME decline visible in Figure 9f. This interaction implies that mixing-chamber design must adopt a coordinated, rather than single-parameter, optimisation strategy—a principle whose generality is consistent with recent multi-parameter optimisations of premixed AWJ nozzles [34].

4.3. Implications for Ultra-High-Pressure AWJ Design

The quantitative parameter ranking (AD > TD > TL > TE) obtained from ANOVA provides a direct design guideline for ultra-high-pressure premixed AWJ mixing-chamber fabrication: AD requires the tightest manufacturing tolerance because of its dominant influence, while TE manufacturing variability is comparatively benign. This priority ordering aligns with the recent industrial-design recommendations of Yuan et al., who emphasised the dominant role of inlet geometry on jet-impact dynamics in high-pressure water-jet ice-cutting applications [20]. with the work of Zhang et al. on waterjet peening, where the inlet-orifice diameter was identified as the most critical determinant of residual stress depth [21,22]. The optimised configuration delivers a measured ME of 34.40%, which exceeds the typical 25–30% range reported for entrainment-type AWJ in earlier comparative studies, confirming the kinetic-energy-transfer advantage of the premixed configuration under ultra-high-pressure operation [35].

4.4. Limitations and Future Work

Several limitations of the present study deserve mention. First, abrasive particles were modelled as non-breakable spheres. Real garnet abrasives possess irregular morphology and may fragment under ultra-high-pressure impact; the Tavares breakage model recently validated in Rocky-DEM by Li et al. for mineral-processing applications offers a promising route for future incorporation [27]. Second, wall erosion was not coupled with the flow simulation; continuous abrasive–wall interaction progressively alters chamber geometry, as recently quantified for premixed AWJ nozzles by Shao [36]. Third, the Standard k–ε turbulence model adopted here, while adequate for bulk mixing prediction, is known to under-resolve flows with strong streamline curvature; comparative RANS-LES studies in similar high-Reynolds-number internal jets suggest that SST k–ω or hybrid models may yield improved local accuracy in the recirculation zones, at the cost of substantially higher computational expense [37]. Finally, the present investigation was restricted to garnet abrasive at fixed grain size; the transferability of the optimised geometry to alternative abrasives and particle-size distributions remains to be verified experimentally.

5. Conclusions

The ultra-high-pressure premixed abrasive waterjet (AWJ) technology offers significant advantages over post-mixed systems, including higher kinetic energy transfer efficiency and simpler structural configuration. However, a critical bottleneck limiting its broader industrial application is the lack of systematic understanding of abrasive-water mixing uniformity under ultra-high-pressure conditions, which fundamentally determines jet cutting and erosion performance. The mixing chamber, as the core component governing this two-phase mixing process, requires coordinated optimization of its geometric parameters to achieve uniform particle distribution. Motivated by this challenge, the present study aimed to establish a quantitative multi-parameter optimization framework for mixing chamber geometry by integrating CFD–DEM numerical simulation with Response Surface Methodology (RSM).

A liquid–solid two-phase flow model of the mixing chamber was developed using the Eulerian k-ε turbulence model coupled with the Fluent-Rocky DEM bidirectional coupling approach. Single-factor numerical simulations were first conducted to identify the effective ranges of five key parameters—mass ratio (MR), throat diameter (TD), throat length (TL), abrasive inlet pipe diameter (AD), and throat exit-to-abrasive inlet pipe center distance (TE)—on mixing efficiency (ME), defined as the cross-sectional area ratio of abrasive particles at the chamber outlet. A four-factor, three-level Box Behnken design was subsequently employed to construct a response surface model and determine the optimal structural parameter combination.

The systematic investigation yielded the following key findings. First, each geometric parameter exhibits a non-monotonic influence on ME, with distinct optimal ranges identified: MR = 25%, TD = 4–5 mm, TL = 12–16 mm, AD = 9–11 mm, and TE = 7–9 mm. Both excessively small and overly large parameter values degrade mixing uniformity through fundamentally different physical mechanisms—excessive jet velocity causing premature particle ejection versus insufficient velocity permitting gravitational settling. Second, the RSM-based ANOVA revealed that AD exerts the dominant influence on ME (F = 36.02), followed by TD (F = 12.61), TL (F = 6.63), and TE (F = 3.61). Importantly, a statistically significant interaction between AD and TE (F = 5.18, $p = 0.0391$) was identified, demonstrating that the optimal abrasive inlet configuration depends on the throat exit geometry—a coupled effect that single-factor analyses cannot capture. Third, under the optimal parameter combination (TD = 4 mm, TL = 12 mm, AD = 10 mm, TE = 7 mm), the simulated ME reached 34.40% $\pm$ 0.49%, in close agreement with the RSM-predicted value of 34.57%. Experimental validation conducted on a premixed AWJ test rig confirmed the reliability of the numerical model, yielding mean absolute relative error of 7.54%, which is below the 10% acceptance threshold for CFD–DEM coupled simulations of liquid–solid two-phase flows. Under the optimum configuration, the moderate throat diameter generates a well-defined central jet core that effectively entrains and accelerates abrasive particles, while the relatively short throat length minimizes wall-induced momentum losses along the acceleration path. The optimized throat exit position enables the vortex structures—formed at the interface between the high-pressure water jet and the incoming abrasive–water mixture—to efficiently capture and disperse particles throughout the mixing chamber cross-section, as illustrated by the transient particle distribution snapshots in Figure 6. The resulting particle velocity field at the outlet exhibits enhanced spatial uniformity, with a narrow velocity distribution indicating that most abrasive particles have been accelerated to velocities approaching that of the water phase. This physical picture explains why the measured ME of 34.40% represents an optimal balance jet momentum, particle residence time, and turbulent dispersion within the ultra-high-pressure mixing chamber.

The findings of this study carry several practical and theoretical implications. From a design perspective, the quantitative ranking of parameter importance (AD > TD > TL > TE) provides clear guidance for prioritizing manufacturing tolerances and dimensional specifications in mixing chamber fabrication. The identification of the significant AD–TE interaction underscores the necessity of coordinated, rather than independent, adjustment of geometric parameters during valve design—a principle that extends beyond the specific configuration studied here. From a methodological standpoint, the demonstrated effectiveness of the coupled CFD–DEM plus RSM framework establishes a transferable optimization paradigm applicable to other solid–liquid two-phase flow components in ultra-high-pressure systems. The experimentally validated optimal configuration serves as a concrete design reference for industrial ultra-high-pressure premixed AWJ systems, with potential applications in mining, tunneling, and advanced manufacturing.

Several limitations of the present study should be acknowledged. The numerical model assumes perfectly spherical and non-breakable abrasive particles, whereas real garnet abrasives possess irregular morphologies and may undergo fragmentation under high-velocity impacts within the mixing chamber. Wall erosion effects, which could progressively alter the optimized chamber geometry during prolonged operation, were not incorporated into the current simulations. Additionally, the investigation was limited to a single abrasive type (garnet), and the optimal parameter values may differ for alternative abrasive materials and operating conditions. Future research should target the integration of particle breakage models, dynamic erosion prediction, and multi-abrasive comparative analyses to enhance simulation fidelity and broaden the applicability of the proposed optimization framework. Long-term operational testing under industrial conditions would further validate the durability and practical robustness of the optimized mixing chamber design.

Author Contributions: H.X. and Y.W. conceptualized the study. H.X. collected resources, identified methods, and applied the software. H.X. and Q.Z. performed the investigation, the data curation and the validation. H.X. and Q.Z. prepared the original draft. H.X. and Y.W. did the review, editing and interpreting the results. All authors have read and agreed to the published version of the manuscript.

Funding: This work was supported by the Scientific Research Start-up Foundation of Anhui University of Science and Technology (Project No. 2024yjrc20).

Institutional Review Board Statement: Not applicable.

Informed Consent Statement: Not applicable.

Data Availability Statement: All relevant data are within the paper, and the authors confirm that the data supporting the findings of this study are available within the article.

Acknowledgments: The authors would like to acknowledge the Institute of Intelligent Machines, Institute of the Chinese Academy of Sciences Hefei Institute of Physical Sciences.

Conflicts of Interest: The authors declare no conflicts of interest.

Abbreviations

The following abbreviations are used in this manuscript:

RSM	Response surface methodology
BBD	Box Behnken design
TD	Throat diameter
TL	Throat length
AD	Abrasive inlet pipe diameter
TE	Distance between the throat exit and the abrasive inlet pipe center
ME	Mixing efficiency

References

1. Tang, J.R.; Lu, Y.Y.; Sun, H.J.; Ge, Z.L.; Xia, B.W.; Li, Q. Study on rock erosion damage characteristics of abrasive jet based on CT method. *Chin. J. Rock Mech. Eng.* **2016**, *35*, 297–302.
2. Wei, J.P.; Xiao, P.W.; Zhang, H.D.; Chen, C.J.; Liu, Y. Study on optimal parameter matching model of abrasive water jet rotary cutting coal and rock. *Coal Sci. Technol.* **2025**, *53*, 192–202.
3. Wei, J.; Du, Y.; Liu, Y.; Wang, M.; Zhao, L. The influence of pulse frequency on the energy evolution law and rock-breaking effect of pulsed abrasive water jet. *Phys. Fluids* **2024**, *36*, 043305. [CrossRef]
4. Ge, Z.L.; Zhao, H.Y.; Lu, Y.Y.; Xiao, S.Q.; Zhou, Z.; Bo, T. Damage and fracture characteristics of coal-sandstone-shale under high-pressure water jet impact. *J. Vib. Shock* **2021**, *40*, 174–181+209.
5. Liu, Y.; Cui, J.; Xu, Z.; Li, Z. Comparison of the rock breakage pressure of abrasive water jets and abrasive air jets. *Geomech. Geophys. Geo-Energy Geo-Resour.* **2020**, *6*, 27. [CrossRef]
6. Hu, Y.; Chen, J.D.; Dai, Q.W.; Huang, W.; Wang, X.L. Development and research status of abrasive jet machining technology. *Surf. Technol.* **2022**, *51*, 80–98.
7. Wang, H.; Yuan, R.; Zhang, X.; Zai, P.; Deng, J. Research Progress in Abrasive Water Jet Processing Technology. *Micromachines* **2023**, *14*, 1526. [CrossRef] [PubMed]
8. Labus, D.A. High pressure equipment and systems. In Proceedings of the 6th WJTA Conference, Houston, TX, USA, 24–27 August 1991; Volume 1A-1–1A-19.
9. Hashish, M. Pressure Effects in Abrasive-Waterjet (AWJ) Machining. *J. Eng. Mater. Technol.* **1989**, *111*, 221–228. [CrossRef]
10. Momber, A.W.; Kovacevic, R. Energy Dissipative Processes in High Speed Water-Solid Particle Erosion. *ASME Int. Mech. Eng. Congr. Expo.* **1995**, *17551*, 555–564. [CrossRef]
11. Oh, T.M.; Cho, G.C. Characterization of Effective Parameters in Abrasive Waterjet Rock Cutting. *Rock Mech. Rock Eng.* **2014**, *47*, 745–756. [CrossRef]
12. Zou, X.; Fu, L.; Wu, L.; Zuo, W. Research on Multiphase Flow and Nozzle Wear in a High-Pressure Abrasive Water Jet Cutting Head. *Machines* **2023**, *11*, 614. [CrossRef]
13. Shi, B.; Pan, J.; Wu, L.; Zhang, X.; Qiu, Y.; Zhang, Y. A Prediction Method of Wear for Volute Casing of a Centrifugal Slurry Pump. *Geofluids* **2020**, *2020*, 8847087. [CrossRef]
14. Li, S.; Shen, Y. Multi-Fluid Modelling of Hydrodynamics in a Dual Circulating Fluidized Bed. *Adv. Powder Technol.* **2020**, *31*, 2778–2791. [CrossRef]
15. Patro, P.; Dash, S.K. Two-Fluid Modeling of Turbulent Particle–Gas Suspensions in Vertical Pipes. *Powder Technol.* **2014**, *264*, 320–331. [CrossRef]
16. Chen, X.; Wang, J. A Comparison of Two-Fluid Model, Dense Discrete Particle Model and CFD-DEM Method for Modeling Impinging Gas–Solid Flows. *Powder Technol.* **2014**, *254*, 94–102. [CrossRef]
17. Zhou, J.W.; Guo, X.L.; Ba, H.; Li, B.; Liu, X.H. Study on flow pattern characteristics of pneumatic conveying in vertical pipeline based on CFD-DEM coupled numerical simulation. *J. Eng. Therm. Energy Power* **2023**, *44*, 2464–2473.
18. Wei, J.; Wang, M.; Yang, H.; Zhang, T.; Du, Y.; Liu, Y. Influence of abrasive mass fraction on rock-breaking effect of premixed abrasive water jet. *J. China Coal Soc.* **2023**, *48*, 251–262.

19. Zhong, L.; Lei, J.; Zuo, Z.; Tu, J.; Deng, J.; Lei, Z.; Zhao, M.; Hua, Y. Simulation analysis of the decontamination effect of different nozzles abrasive jet based on CFD-DEM. *Part. Sci. Technol.* **2023**, *41*, 864–875. [CrossRef]
20. Yuan, G.Y.; Ni, B.Y.; Liu, P.; Kim, D.K. Ice Damage Characteristics Under High-Pressure Water Jet Based on Johnson–Holmquist II Brittle Constitutive Model. *Phys. Fluids* **2025**, *37*, 086153. [CrossRef]
21. Zhang, P.; Gao, Y.; Zhang, J.; Yue, X.; Zhou, H.; Sun, Y. The Influence Mechanism of Water Jet Peening on the Fatigue Crack Growth Behavior of 7075 Aluminum Alloy. *Int. J. Fatigue* **2024**, *187*, 108429. [CrossRef]
22. Zhang, P.; Yue, X.; Sun, Y.; Zhou, H.; Zhang, J.; Wang, Y. Ultrasonic Peening-Waterjet Composite Surface Modification of 7075-T6 Aluminum Alloy for Residual Stress Release and Transformation Mechanism. *J. Alloys Compd.* **2024**, *1002*, 175181. [CrossRef]
23. Chen, Y.X.; Zhang, Z.J. Simulation study on particle-bubble interaction behavior based on discrete element method. *J. China Coal Soc.* **2023**, *48*, 1403–1412.
24. Zhang, F.T.; Zhang, J.; Wu, Y.W.; He, Y.N.; Tian, W.X.; Qiu, S.Z. CFD-DEM-Based Fluid–Solid Coupling Numerical Simulation of Containment Debris Migration. *At. Energy Sci. Technol.* **2024**, *59*, 1284–1293.
25. Cai, G.Q.; Diao, X.F.; Yang, R.; Wang, B.C.; Gao, S.; Liu, T. Research Progress on Fluid–Solid Coupling Numerical Modeling Methods Based on CFD-DEM. *J. Harbin Inst. Technol.* **2024**, *56*, 17–32.
26. Launder, B.E.; Spalding, D.B. Paper 8—The Numerical Computation of Turbulent Flows. In *Numerical Prediction of Flow, Heat Transfer, Turbulence and Combustion*; Pergamon Press: Oxford, UK, 1983; pp. 96–116.
27. Li, P.; Zhou, L.; Liu, S.; Wang, J.; Wang, J.; Cao, Z. Evaluation of Grinding Media Type Using DEM Simulations with Tavares Breakage Model. *Powder Technol.* **2025**, *460*, 121064. [CrossRef]
28. Tang, J.; Zhang, J.; Liu, W.; Chen, C.; Zhang, H.; Cui, J. Two-Way Coupled CFD-DEM Model of a Pre-Mixed Abrasive Water Jet and Its Application to the Investigation of Abrasive Motion Characteristics. *Powder Technol.* **2024**, *438*, 119650. [CrossRef]
29. Zhang, X.; Wang, Y.; Xie, H.; Zhang, G. Cutting Surface Roughness Prediction Model for Cutting Carbon Steel Using Premixed Abrasive Water Jet. *Int. J. Adv. Manuf. Technol.* **2024**, *133*, 1185–1199. [CrossRef]
30. Wang, H.; Huang, C.; Shi, Z.; Huang, S.; Li, Y.; Wang, Z.; Xu, L.; Qu, M.; Xu, Z.; Zhang, D. Surface Integrity Improvement of the 316L Stainless Steel Manufactured by Selective Laser Melting Using a Pre-Mixed Abrasive Water Jet Method. *Mater. Today Commun.* **2025**, *46*, 112666. [CrossRef]
31. Javadpour, S.M.; Kadivar, E.; Zarneh, Z.H.; Kadivar, E.; Gheibi, M. Optimizing droplet coalescence dynamics in microchannels: A comprehensive study using response surface methodology and machine learning algorithms. *Heliyon* **2025**, *11*, e41510. [CrossRef]
32. Liu, Y.; Chen, X.; Zhang, J.; Feng, L.; Liu, H.; Hao, C. Structural optimization design of ice abrasive water jet nozzle based on multi-objective algorithm. *Flow Meas. Instrum.* **2024**, *97*, 102586. [CrossRef]
33. Fuse, K.; Chaudhari, R.; Vora, J.; Patel, V.K.; de Lacalle, L.N. Multi-Response Optimization of Abrasive Waterjet Machining of Ti6Al4V Using Integrated Approach of Utilized Heat Transfer Search Algorithm and RSM. *Materials* **2021**, *14*, 7746. [CrossRef]
34. Schwartzentruber, J.; Narayanan, C.; Papini, M.; Liu, H.T. Optimized Abrasive Waterjet Nozzle Design Using Genetic Algorithms. In Proceedings of the 23rd International Conference on Water Jetting, Seattle, DC, USA, 16–18 November 2016.
35. Natarajan, Y.; Murugesan, P.K.; Mohan, M.; Liyakath Ali Khan, S.A. Abrasive Water Jet Machining process: A state of art of review. *J. Manuf. Process.* **2020**, *49*, 271–322. [CrossRef]
36. Shao, C.; Ge, Z.; Zhou, Z.; Liu, W.; Li, Z.; Tian, C.; Chang, W. Experimental and numerical investigation of abrasive water jet nozzle erosion. *Powder Technol.* **2023**, *430*, 119031. [CrossRef]
37. Hlaváč, L.M.; Hlaváčová, I.M.; Jandačka, P.; Zegzulka, J.; Viliamsová, J.; Vašek, J.; Mádr, V. Comminution of Material Particles by Water Jets—Influence of the Inner Shape of the Mixing Chamber. *Int. J. Miner. Process.* **2010**, *95*, 25–29. [CrossRef]